# Dependence of fast-ion transport on the nature of the turbulence in the Large Plasma Device

Shu Zhou,[1] W. W. Heidbrink,[1] H. Boehmer,[1] R. McWilliams,[1] T. A. Carter,[2] S. Vincena,[2] and S. K. P. Tripathi [2]
[1]*Department of Physics and Astronomy, University of California, Irvine, California 92697, USA*
[2]*Department of Physics and Astronomy, University of California, Los Angeles, California 90095, USA*

(Received 19 June 2011; accepted 14 July 2011; published online 11 August 2011)

Strong turbulent waves ($\delta n/n \sim 0.5$, $f \sim 5$-$40$ *kHz*) are observed in the upgraded Large Plasma Device [W. Gekelman, H. Pfister, Z. Lucky, J. Bamber, D. Leneman, and J. Maggs, Rev. Sci. Instrum. **62**, 2875 (1991)] on density gradients produced by an annular obstacle. Energetic lithium ions ($E_{fast}/T_i \geq 300$, $\rho_{fast}/\rho_s \sim 10$) orbit through the turbulent region. Scans with a collimated analyzer and with probes give detailed profiles of the fast ion spatial distribution and of the fluctuating wave fields. The characteristics of the fluctuations are modified by changing the plasma species from helium to neon and by modifying the bias on the obstacle. Different spatial structure sizes ($L_s$) and correlation lengths ($L_{corr}$) of the wave potential fields alter the fast ion transport. The effects of electrostatic fluctuations are reduced due to gyro-averaging, which explains the difference in the fast-ion transport. A transition from super-diffusive to sub-diffusive transport is observed when the fast ion interacts with the waves for most of a wave period, which agrees with theoretical predictions. © *2011 American Institute of Physics*. [doi:10.1063/1.3622203]

## I. INTRODUCTION

The transport of fast ions in electrostatic microturbulence is important in natural and laboratory plasmas. Fast ions are ions with much larger energy than typical thermal plasma ions. In magnetically confined plasmas, fast ions can be generated by fusion reactions and by auxiliary heating. The confinement of fast ions is critical in fusion experiments approaching ignition. The question of whether and to what extent these fast ions are affected by electrostatic microturbulence has attracted growing interest in recent years. While a number of simulations[1–4] reported fast ion transport in slab or toroidal geometry, the experimental study on this topic is very challenging because of the difficulty in diagnosing the fast ion population and turbulent wave fields accurately. Experimental results reported in tokamaks confirms that, in the high energy regime (the ratio of fast ion energy to thermal ion energy $E_{fast}/T_i >> 10$), ions are well confined in electrostatic microturbulence (see, e.g., Ref. 5 and references therein). But anomalous transport at small $E_{fast}/T_i$ has been reported.[6–10] However, quantitative comparison between tokamak experiments and simulations is difficult due to the indirect and limited fast ion diagnostic abilities in hot plasmas. Several experimental works[11–13] in a basic linear device reported that ion heating and transport is enhanced under large electrostatic fluctuations. Measurement of energetic particles in a toroidal magnetized basic plasma device (TORPEX) has also begun.[14,15]

The fast ion campaign at the upgraded Large Plasma Device[16] (LAPD) at the University of California, Los Angeles has been focused on understanding fast ion transport mechanisms in various background waves in a basic linear device. Several experiments has been conducted and reported, including study of fast ion classical transport[17] and study of Doppler-shifted resonance of fast ions with linearly[18] or circularly[19] polarized shear Alfvén waves (SAW). LAPD provides a probe-accessible plasma with direct and accurate diagnostic tools. Its large dimensions, which are comparable to magnetic fusion research devices, accommodate long-wavelength modes and large fast-ion gyro-orbits.

In this paper, we report the direct measurements of fast-ion transport in the presence of electrostatic waves with various characteristics in the LAPD. An earlier work[20] reported the energy scaling of fast-ion transport in drift-wave turbulence induced by a half-plate obstacle. However, the fast-ion orbits were only partially immersed in waves due to the geometry of the obstacle, and the wave characteristics were not modified. In the current experimental setup, the gyro-radius is kept constant, and the dependence of the fast-ion transport on the background turbulent wave characteristics, such as correlation length and perpendicular wavelength, are studied. An annular obstacle is placed in the LAPD chamber to block primary electrons from the cathode-anode source. The obstacle induces large density gradients with cylindrical geometry downstream and destabilizes the waves. Modification of wave characteristics is done by changing the plasma species and by biasing the obstacle at different voltages. Coherent and turbulent waves with various mode numbers are observed in helium and neon plasmas. The approach to study the fast ion transport in these waves is to launch a test-particle fast ion beam with narrow initial radial width. The trajectories of the fast ions orbit through the potential structures of the turbulent waves. A collimated fast ion collector is inserted into the chamber at various distances away from the ion source to collect fast ion signals.

Here we summarize the primary results reported in this paper. The fast ion beam cross-field transport measured for coherent waves (with long azimuthal correlation length and coherent mode structures) is at the classical level, indicating that wave-induced transport is small due to the large gyro-orbit

 

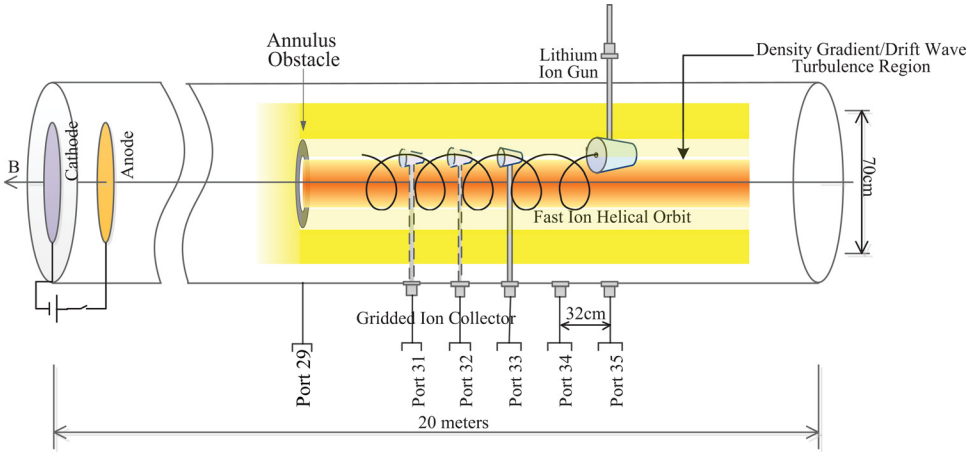


FIG. 1. (Color online) Schematic of LAPD including the annular obstacle, the lithium ion gun, and the ion collector. The ion collector is inserted at various axial locations to study the spatial dependence of the beam transport. The ion gun and collector are axially aligned and operated at the same pitch angle. Fast ion beam orbits are helical and fully overlapped with the steep gradient region.

of fast ions. Fast-ion transport increases in waves that have a larger scale size. Turbulent waves (with short azimuthal correlation) induce more fast-ion transport than coherent waves when the wave scale sizes are about the same. The time variation of fast-ion beam diffusivity indicates that a transition from super-diffusive to sub-diffusive transport occurs when the fast ion interacts with the waves for most of a wave period. The observed experimental results are explained well both by gyro-averaging theory and by a Monte-Carlo test particle following code. This paper mainly describes the fast-ion beam behavior in various electrostatic wave fields, while a companion paper will present detailed analysis on the wave instability and associated thermal transport modified by the bias-induced edge shear flow and the strength of the axial magnetic field.

The organization of this paper is as follows: The experimental setup and basic plasma parameters are introduced in Sec. II. Major experimental results including measurement of fast ion transport in background waves with various correlation lengths ($L_{corr}$) and structure sizes ($L_s$) are reported in Sec. III. In Sec. IV, the time dependence of the observed fast ion beam diffusivity is discussed. Conclusions are drawn in Sec. V.

## II. EXPERIMENTAL SETUP

### A. Overview

The experiment is performed in the upgraded Large Plasma Device (LAPD) at UCLA. LAPD is an 18-m-long, 1-m-diameter cylindrical vacuum chamber, coaxial with 56 solenoid magnetic field coils. The axial magnetic field in this experiment is uniform with $B_z \sim 1200$ Gauss. Pulsed plasmas with ~10 ms duration are created using a barium oxide coated cathode source at 1 Hz repetition rate. During the pulse time, a 40-60 V bias is applied between the cathode and anode, resulting in ~4 kA of discharge current. Primary electrons with energy comparable to the cathode-anode bias voltage are generated during the discharge. These primary electrons flow downstream along the axial magnetic field lines and lead to ionization in the main chamber. The plasma column has a diameter of $\leq$70 cm. The working gases used in this experiment are helium and neon. Typical parameters during the active discharge in a helium plasma (at a fill pressure of $\sim 2 \times 10^{-4}$Torr) are $n_e \sim 2.5 \times 10^{12}\text{cm}^{-3}$, $T_e \sim 5\,eV$, $T_i \sim 1$ eV. Measurements of plasma density, floating potential, temperature, and their fluctuations are made using Langmuir probes.[21] The experimental setup is shown schematically in Fig. 1. A copper, annular obstacle with inner radius of 6 cm and outer radius of 10 cm is inserted upstream (port 29), concentrically with the plasma column. When placed, the obstacle blocks the plasma-forming primary electrons parallel to the magnetic field, and significantly decreases the downstream plasma density. A steep density gradient, along with large density fluctuations, is observed on the inner edge region of the annular depletion. Figure 2 shows a typical radial profile of the plasma density $n_e$ and root-mean-square (rms) of ion saturation current $I_{sat}$ fluctuation amplitude measured 0.3 m downstream from the annulus during the ~10 ms plasma discharge. The annular obstacle is either floating or positively biased relative to the LAPD anode using a dc biasing power supply.

The lithium ion gun[22,23] is inserted into the LAPD plasma at port 35 with variable pitch angle to the axial magnetic field. The initial width of the lithium ion beam is limited by the exit aperture of the gun (~5 mm), while the beam energy is set by the biasing voltage between the lithium emitter and the molybdenum grid on the aperture. The fast ion energy in this experiment ranges from 300 eV up to 600 eV. The angular divergence of the beam is $\sim\pm 5^\circ$, with energy divergence ~5 eV. The ion beam trajectories are helical: parallel motion along the magnetic field with constant velocity $v_z$, and gyro motion perpendicular to the magnetic field. The gyro-radius of the beam perpendicular motion is set to be 5.7 cm, which is slightly smaller than the inner radius (6 cm) of the annular obstacle (red dashed line in Fig. 2(a)). Thus the beam trajectories fully overlap with large plasma density and potential fluctuations. A collimated fast ion collector is inserted at three axial locations (port 31-33, with axial distance of 64-128 cm from the source) to measure the beam spreading as a function of its time-of-flight in waves. The fast-ion orbit is carefully designed so that the fast ions finish integer number of orbits before they are collected. In this way, the initial slightly divergent beam is refocused at each observation point. The lithium ion source and

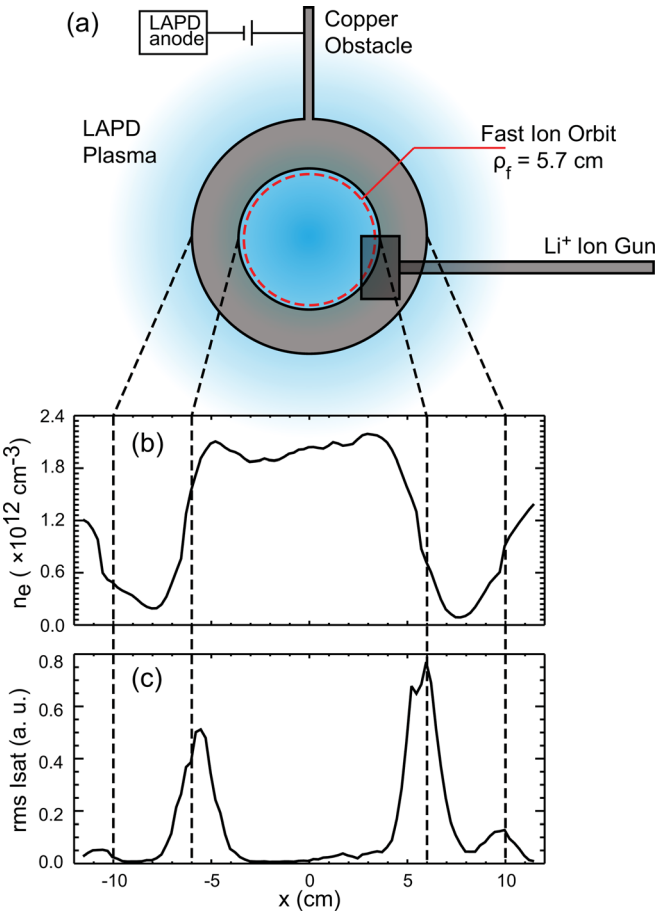


FIG. 2. (Color online) (a) Schematic of the LAPD end-view. Fast ion gyro-orbit (dashed line) overlaps with the steep gradient region. The copper obstacle can be biased positively related to the LAPD anode by an external power supply. (b) Typical plasma density profile. (c) Typical root-mean-square (RMS) fluctuation of the ion saturation current.

collector were tested and successfully used in several previous experiments.[18,20]

### B. Waves associated with an annular obstacle

Several theoretical[24] and experimental[25,26] works in LAPD are focused on characterizing the so-called drift-Alfvén waves associated with steep density gradient. In the current experiment, the observed plasma density gradient 0.3 m downstream from the inner edge ($x = \pm 6$ cm) of the obstacle has a transverse scale length $L_n = |\nabla \ln n|^{-1} \sim 2$ cm (the background ion sound gyroradius in helium plasma is $\rho_s = 0.6$ cm, and the ion gyro-radius $\rho_i \sim 0.24$ cm). The typical plasma density and potential fluctuations observed have similar amplitude ($\delta n/n \sim e\tilde{\phi}/kT_e \sim 0.5$). The parallel wavelength $\lambda_{||}$ of the fluctuation is measured by two Langmuir probes aligned axially and separated by 2.2 m. A phase difference of 50° is observed between the $I_{sat}$ signals of the two probes, indicating that $\lambda_{||} \sim 15$ m, which is comparable to the LAPD machine length. The long and finite parallel wavelength is expected in a drift-wave like turbulence. Measurements with a B-dot probe indicate that the fluctuation in ambient magnetic fields is $\delta B/B \sim 0.2\%$.

Several means are employed to change the wave characteristics such as mode numbers ($m$) and spatial correlation length ($L_{corr}$). Driving azimuthal $E \times B$ flow has been reported as an effective way to modify the LAPD edge turbulence in a wall-biasing experiment.[27] A similar setup is used here to bias the annular obstacle positively relative to the LAPD anode. With the obstacle biased, a plasma potential gradient is observed downstream and large $E \times B$ drift in the azimuthal direction is driven ($v_{E\times B}/v_s \sim 0.5$, where $v_s$ is the ion sound velocity, measured using a Mach probe). Other ways to modify the wave scale size are to use different plasma species and to modify the amplitude of the axial magnetic field. Density and potential fluctuations under a broad range of the obstacle biasing voltage, plasma species, and axial magnetic field strength have been documented, and several typical cases with varied scale lengths are selected for the fast-ion transport study. A detailed discussion on the wave instabilities and the associated thermal transport is reported elsewhere,[28] so only a brief summary is given here. In cases with low obstacle-bias voltage ($V_{bias}$) and large axial magnetic fields ($B_z$), improved thermal plasma confinement is observed, along with steeper edge density gradients. The radially sheared flow induced by $E \times B$ drift dramatically changes the cross-phase between density and potential fluctuations, which causes the wave-induced particle flux to reverse its direction across the shear layer and forms a transport barrier. In cases with higher $V_{bias}$ or smaller $B_z$, large radial transport and rapid depletion of the central plasma density are observed. Two-dimensional cross-correlation measurements show that a mode with azimuthal mode number $m = 1$ and large radial correlation length dominates the outward transport in these cases.

Three typical wave conditions with different azimuthal correlation length $L_{corr}$ and potential structure scale length $L_s$ (parameters listed as cases (A)-(C) in Table I) are chosen for the fast-ion transport study: (A) in helium plasma with the annulus floating; (B) in helium plasma with the annulus biased at 100 V relative to LAPD anode; and (C) in Neon plasma with annulus biased at 75 V. Figure 3(a) shows a two-dimensional (2D) cross-field correlation function for $I_{sat}$ fluctuations in case (A), measured using two triple probes separated along the magnetic field by 0.3m. $L_{corr}$ is defined as the azimuthal scale length of the wave cross-correlation function, and $L_s \sim \pi\rho_f/\bar{m}$ is the scale size of a wave density/potential structure, with $\bar{m}$ the average mode number and $\rho_f$ is the fast-ion gyroradius. In fully turbulent fluctuations, $L_{corr} \sim L_s$ (case (B)), while in coherent waves $L_{corr}$ can be much longer than $L_s$ (case (A)). It is assumed here that density and potential fluctuations have similar scale size in

TABLE I. Wave characteristics for the four cases with complete fast-ion data.

| Case # | Plasma | $V_{annulus}$ (V) | $n_e(\times 10^{12}\,\mathrm{cm}^{-3})$ | $\delta n/n$ | $e\tilde{\phi}/kT_e$ | $\bar{m}$ | $L_s$(cm) | $L_{corr}$(cm) |
|---|---|---|---|---|---|---|---|---|
| A | Helium | Floating | 2.2 | 0.55 | 0.46 | 7 | 2.6 | 23 |
| B | Helium | 100 | 2.0 | 0.53 | 0.48 | 7 | 2.6 | 6 |
| C | Neon | 75 | 1.4 | 0.35 | 0.47 | 2 | 6.3 | 19 |
| D | Helium | Floating | 2.0 | 0.30 | 0.30 | 7 | 2.6 | 7 |

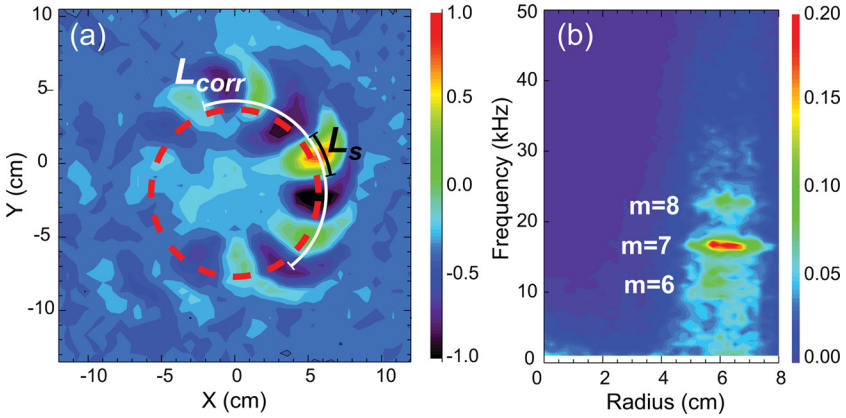


FIG. 3. (Color online) (a) Two-dimensional cross-field correlation function for $I_{sat}$ in case A, with the wave azimuthal correlation length ($L_{corr}$) and structure scale size ($L_s$). The asymmetry in the correlation pattern is caused by the decorrelation of the signals between the reference probe (located at (6,0) in (a)) and the moving probe. (b) Contour of the spatially resolved wave spectrum for this case. The dominant modes are m = 6-8.

drift-wave like turbulence. The power spectrum contours and 2D correlation functions of $I_{sat}$ in all three cases are compared. In helium plasmas, when the annulus is floating (Fig. 3), the observed waves are very coherent, with mode number dominated by $m = 6 - 8$ ($L_s \sim 2.6$ cm), and have relatively long azimuthal correlation length ($L_{corr} \sim 23$ cm). When the annulus is biased to 100 V, the waves (Fig. 4) are more turbulent. The azimuthal correlation length is changed significantly ($L_{corr} \sim 6$ cm), and the $I_{sat}$ power spectrum is closer to broadband. $L_s$ in this case is similar to case (A). In neon plasmas with 75 V bias on annulus, waves with mode number $m = 1 - 3$($L_s \sim 6.3$ cm) and long azimuthal correlation ($L_{corr} \sim 19$ cm) are observed (Fig. 5).

## III. FAST-ION TRANSPORT IN VARIOUS BACKGROUND WAVES

### A. Observed beam broadening in waves

A $^7$Li ion beam with energy $E = 575$ eV and pitch angle $\theta_{pitch} = 48°$ is launched and collected at several positions (64 cm, 96 cm, 128 cm away from the source) to obtain the beam transport due to the background waves that were described in the previous section. Beam 2D profiles are obtained by time-averaging over the collector signal taken at a selected spatial grid. The broadening of the beam profiles in the radial (along the gyro-radius) direction indicates cross-field transport. The spatial-averaged radial profile is fitted into a Gaussian function to quantify the beam full-width at half-maximum (FWHM). The beam broadening in the azimuthal direction (along the gyro-orbit) is not accurately measured, due to the limited angular acceptance of the collimated collector.[20] Thus only the radial profiles of the beams are analyzed.

To quantify the fast ion transport due to interaction with drift-wave turbulence, the classical transport by Coulomb collisions with the background plasmas (dominated by ion-ion pitch angle scattering) is estimated and subtracted. The classical diffusion of fast ion beams in LAPD is well understood[17] and a Monte-Carlo (MC) code simulates the beam broadening due to classical effects. Another indicator of the classical diffusion effect is the beam FWHMs in early afterglow plasmas (<10 ms after the discharge ends). When LAPD discharge is terminated, the electron temperature ($T_e$) decays rapidly, while the plasma density ($n_e$) drops on a much slower timescale. In the early afterglow ($n_e$ drops by $\leq 20\%$, $T_e \leq 1$ eV), the ambient plasma is quiescent relative to the active discharge, and fast-ion cross-field transport is mainly due to classical Coulomb collisions. The beam FWHM measured in the early afterglow is compared with the simulation result obtained by the MC code and shows good agreement in both helium and neon plasmas (Fig. 6).

Fast ion beam profiles in LAPD active discharges ($n_e \sim 2.5 \times 10^{12}$ cm$^{-3}$, $T_e \sim 5$eV) indicate both classical transport and transport due to interaction with low-frequency wave potential fields. Beam profiles in various background waves (cases (A)-(C)) are compared (Fig. 7). When the background waves are azimuthally coherent and with a large

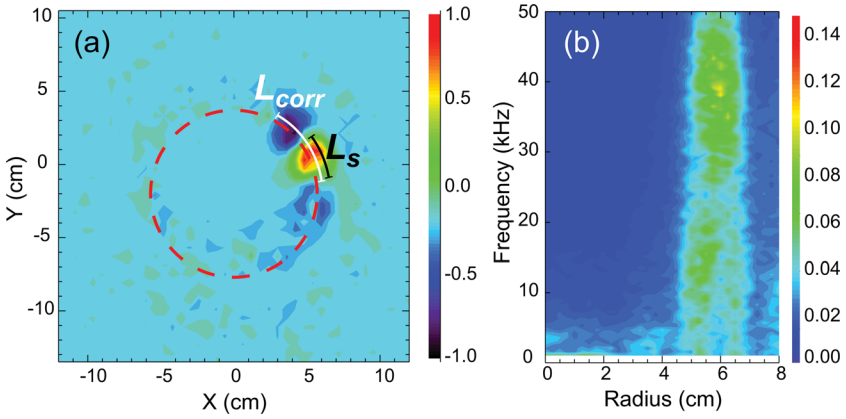


FIG. 4. (Color online) (a) Two-dimensional cross-field correlation function for $I_{sat}$ in case (B). (b) Contour of the spatially resolved wave spectrum for this case. The waves have average mode number $\bar{m} = 7$, short azimuthal correlation length and are broadband.

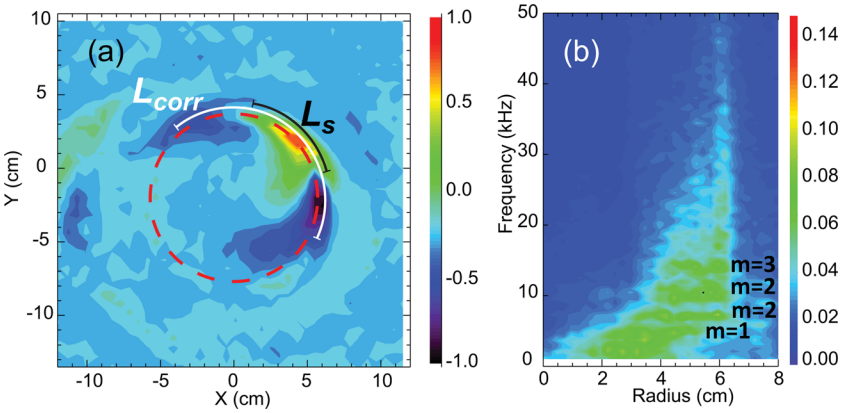


FIG. 5. (Color online) (a) Two-dimensional cross-field correlation function for $I_{sat}$ in case (C). (b) Contour of the spatially resolved wave spectrum for this case. The dominant modes are $m$=*1-3*.

mode number (case (A), red triangles), the beam radial FWHMs are comparable to the classical transport level, indicating that the wave induced transport is very small. In contrast, when in waves with small mode number and large structure size (case (C), blue diamonds), beam radial FWHMs greatly exceed the classical diffusion level, indicating that wave-particle interaction dominates the beam broadening. Two cases with similar averaged mode number, but very different correlation length $L_{corr}$ (cases (A) and (B)) also have different levels of transport. A more broadband wave with shorter $L_{corr}$ (case (B), red circles) induces larger beam broadening.

### B. Reduced fast ion cross-field transport by gyro-averaging

The difference of beam broadening in various background waves can be explained by the gyro-averaging effect. It is predicted[1,2] that fast ion transport in electrostatic waves is much smaller than that of thermal ions because the large orbit size phase-averages over turbulent potential structure which typically has a scale length comparable to the thermal ion gyro radii.[29] The gyro-averaged electrostatic potential is

$$\bar{\phi}(x) = \sum_k \phi_k e^{ik\cdot x} J_0(k\rho_f), \tag{1}$$

where $\phi_k$ is the potential in $k$ space, $\rho_f$ is the fast ion gyro radius, and $\bar{\phi}$ is the potential that is reduced by averaging over

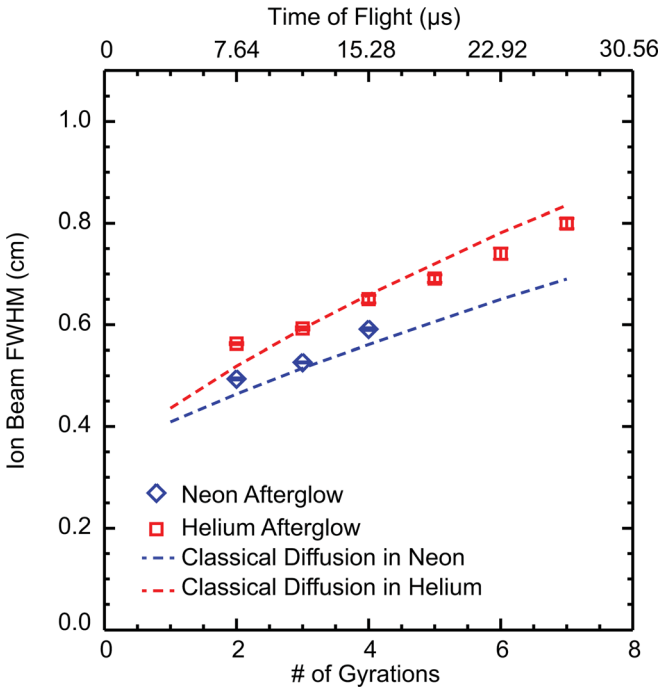


FIG. 6. (Color online) Spatial-temporal evolution of the fast-ion beam full-width at half-maximum (FWHM) in LAPD afterglow in Helium (square) and Neon (diamond) plasmas. Classical diffusion levels in these cases (dashed lines) are simulated by a Monte-Carlo code and agrees well with the experimental data.

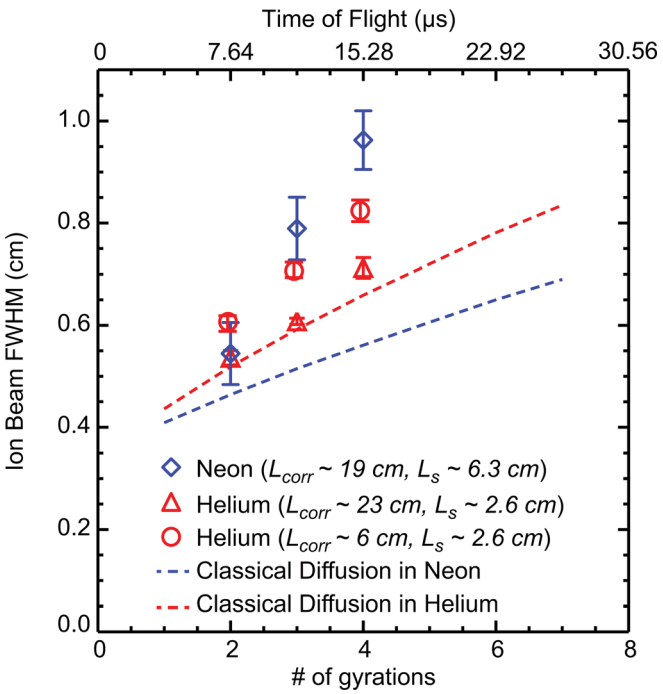


FIG. 7. (Color online) Spatial-temporal evolution of the fast-ion beam FWHM during LAPD discharge when the fast ions overlap with the waves described in cases (A)-(C). The simulated classical diffusion (dashed lines) is also plotted.

the gyro-orbit. The equation shows that the gyro-averaged potential depends on the amplitude and spatial spectrum of fluctuating potential ($\phi_k$), and the ratio of fast-ion orbit size ($\rho_f$) to wave potential structure size ($k^{-1}$). In this paper, experimental results regarding the dependence of fast-ion transport on these parameters are discussed.

In the previous shear-Alfvén-resonance experiment, it was reported that the fast ion beam is weakly affected by magnetic fluctuations with $\delta B/B \sim 1\%$ unless the Doppler-shifted cyclotron resonance condition is satisfied.[19] Therefore, in this investigation, the beam broadening due to magnetic fluctuation can be neglected, and the ambient wave can be treated as electrostatic. Two effects could induce fast ion cross-field transport in low-frequency electrostatic waves: the change of fast ion gyro-radius due to energy exchange with waves, and the gyro-center (GC) drifts due to turbulent electric fields. One may estimate the energy exchange between fast ions and the wave potential during one gyro orbit by

$$\delta E_\perp \sim e\delta\phi \sim kT_e \cdot \delta n/n \sim 0.5kT_e,$$

and the resulting change in gyro-radius is

$$\delta\rho_f \sim \frac{1}{\Omega_f}\left(\sqrt{\frac{2(E_\perp+\delta E_\perp)}{M_f}}-\sqrt{\frac{2E_\perp}{M_f}}\right) \sim \rho_f\frac{KT_e}{4E_\perp} \sim 0.0035\rho_f \sim 0.02\,\text{cm}.$$

And the gyro-center $E \times B$ drift during one gyro-period is

$$\delta l \sim \frac{\nabla\delta\phi}{B_0}\cdot\frac{2\pi}{\Omega_f} \sim 0.2\,\text{cm}.$$

So the fast ion beam broadening is mainly the result of the gyro-center drifts in the electrostatic wave potential.

The predicted effect of the gyro-averaged fast ion gyro-center drifts are illustrated by plotting a test particle GC trajectory (Fig. 8) in an experimentally measured coherent wave field (waves in case (A)). Due to the time scale separation between the fast ion cyclotron frequency and the characteristic frequency of the waves ($\Omega_f >> \omega_{DW}$), the fast-ion samples nearly static azimuthal potential structures during each gyro-orbit. The scale length of the test particle GC drift through one potential structure is $\sim$0.2 cm. In waves with long $L_{corr}$, the $E \times B$ drifts cancels each other when the beam orbit passes through the coherent potential structures. So the total drift averaged over the gyro-orbit is greatly reduced compared to that in a stochastic potential field.

An estimate of the gyro-averaging effect in different observed background wave fields is illustrated in Fig. 9. The wave potential structures for cases (A)-(C) are modeled by

$$\phi(r,\theta,t) = \sum_m \phi_m \cdot \sin(m\theta+\omega t+\theta_0)e^{\left(-\frac{(r-r_0)^2}{a}\right)} \quad (2)$$

with $m = 6-8$ for case (A) and $m = 1-3$ for case (C). Nonlinear simulation is required to model the fully turbulent potential fields in case (B). However, the effect of the turbulent waves to the fast-ion transport can be demonstrated roughly by waves with more modes ($m = 5-9$). The averaged potential $\bar{\phi}(r,\theta,t)$ over a gyro-orbit is obtained using Eq. (1). The wave amplitudes in all cases are kept the same. The ratios of fluctuating amplitude after gyro-averaging to the original amplitude ($|\bar{\phi}_{A,B,C}|/|\phi_0|$) indicate the effectiveness of the gyro-averaging for different wave characteristics. For case (A), $|\bar{\phi}_A|/|\phi_0| < 0.1\%$, indicating a large reduction of fast-ion-sampled wave amplitude due to the coherency and small scale size of the waves. For case (C), $|\bar{\phi}_C|/\ |\phi_0| \sim 5\%$, which shows that waves with larger scale

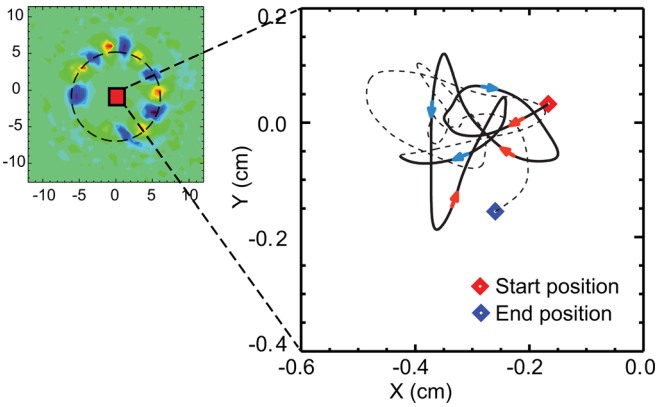


FIG. 8. (Color online) The trajectory of a test particle gyro-center (GC) in coherent wave potential fields. The potential structure is inferred from the cross-correlation function of $I_{sat}$ for case (A).

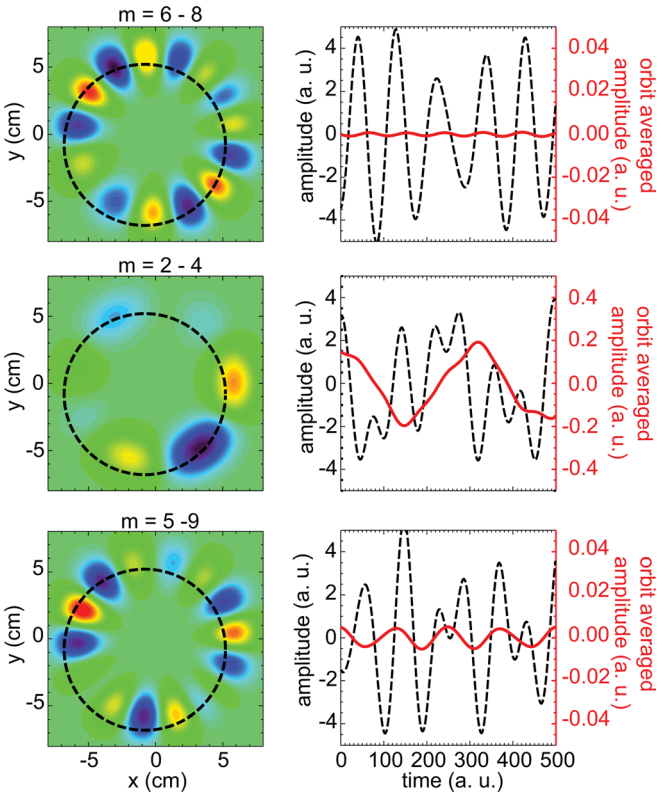


FIG. 9. (Color online) (Left) Wave potential fields with characteristics similar to the experimental cases (A)-(C), modeled by Eq. (2). (Right) Original potential fluctuation (black dashed line) and fluctuation after orbit-averaging (red solid line) over the indicated gyro-orbit.

size contribute more to the fast-ion transport. The fast-ion transport in fully turbulent waves (case (B)) is expected to be enhanced compared to that in coherent waves with the same scale size. Because of the short decorrelation length of the turbulent structure, fast-ion guiding-center $E \times B$ drift in turbulent waves is more stochastic. A rough estimate by calculating the averaged $|\bar{\phi}_B|$ in potential fields with $m = 5 - 9$ shows that $|\bar{\phi}_B|/|\phi_0| \sim 0.2\%$, which is larger than $|\bar{\phi}_A|/|\phi_0|$ and is consistent to our expectation. The analysis above indicates that the scale size (or average mode number $\bar{m}$) of the waves is the major influence factor on the gyro-averaging effect, while turbulent waves induces more fast-ion transport than coherent waves when $\bar{m}$ is about the same for the two cases. This agrees well with the experimental results.

## IV. TIME DEPENDENCE OF FAST ION DIFFUSIVITY IN WAVES

### A. Observed transition from super-diffusive to sub-diffusive transport

The perpendicular diffusivity ($D_\perp$) of the fast-ion beam in background electrostatic wave fields is generally space and time dependent. In our analysis, the spatial dependence of $D_\perp$ is neglected because the turbulent wave structures observed in this experiment have a parallel wavelength much longer than the axial distance travelled by a fast-ion ($\lambda_\parallel \sim 15$ m, while the maximum axial distance a fast-ion travels is ~1.27 m). Thus the background wave structure is approximately flute-like, and $D_\perp$ only depends on the fast-ion time-of-flight in waves. The time-dependence of the fast ion beam diffusivity can be generally written as $D_\perp \propto t^\gamma$. In diffusive transport, $D_\perp$ is independent of time and $\gamma = 0$. Transport with $\gamma > 0$ is described as super-diffusive, while transport with $\gamma < 0$ is sub-diffusive. In the current experiment, the modification of the fast-ion gyro-radius due to its energy change can be neglected, as discussed above. Thus the time variation of the collected beam FWHMs directly reflects the transport of the fast-ion gyro-centers. Two important characteristic time scales[30] decide the nature of the fast ion diffusivity in low-frequency electrostatic waves: the wave-particle decorrelation time ($\tau_c$), and the time scale for the waves to change their phase ($\tau_{ph}$). Here, $\tau_{ph} \sim \bar{L}_s/v_{dr}$ is defined as the phase changing scale time of the wave structures, where $\bar{L}_s$ is the averaged azimuthal potential scale length and $v_{dr}$ is the wave azimuthal phase velocity. In coherent waves, $\tau_{ph}$ is comparable to half of the wave period ($\pi/\omega$). Since the fast ion cyclotron frequency is much larger than any of the wave timescales, $\tau_{ph}$ is also the amount of time that a fast ion samples the same phase of the wave. When the fast ion time-of-flight in the waves is short ($T_f << \tau_{ph}$), the background wave can be treated as a static potential field, and the fast ions sample the same wave fields during every gyro-orbit. The collective beam transport is then super-diffusive, with diffusivity linearly growing with time ($D_\perp \propto t$). When $T_f \sim \tau_{ph}$, sub-diffusive transport is expected: The fast ion starts to sample different phases of the wave potential, and $D_\perp$ decreases with time. Diffusive transport ($D_\perp = const$) only happens when the fast ion orbit is fully decorrelated with the initial wave field ($T_f > \tau_c$) and its motion in the waves becomes stochastic.

The time dependence of the fast-ion transport in drift waves associated with a plate obstacle was discussed in an earlier publication.[20] Super-diffusive (ballistic) transport was observed, since the fast-ion time-of-flight in wave was much shorter than any of the wave time scales. In other words, long-time wave-particle interaction was not achieved. In the present experiment, the ion gun and collector are operated in a slightly different manner so that the fast ion beam samples the waves for a longer time. The axial distance of fast ion travelling in the waves is limited by the distance between the ion gun and the obstacle (~1.5 m). However, the wave-particle interaction time can be varied by increasing the pitch angle of the ion beam while keeping $\rho_f$ a constant (Fig. 10). Since the fast ion cyclotron frequency ($\Omega_f$) is constant, the time-of-flight of the fast ion before it is collected is

$$T_f = \frac{L}{v_z} = \frac{L}{\sqrt{2E_\perp/M_{Li^+}}} \tan(\theta_{pitch}),$$

where $L$ is the total axial distance between the ion gun and collector and $\theta_{pitch}$ is the pitch angle of the fast ion beam. The fast ion perpendicular energy is kept constant at $E_\perp = 320$ eV, (with $\rho_f = 5.7$ cm) so that the beam trajectories always overlap with the same wave field. By operating the gun at higher pitch angles (up to $\sim 80°$), the fast ion time-of-flight in the waves is greatly extended.

Fast ion beam profiles with the averaged number of gyro-orbits $\bar{n}_{gyro} = 4 \sim 22$ are obtained in helium plasmas with the annular obstacle floating. The fast-ion gun is located at port 35, while the collector is at port 31. The axial distance between the gun and the collector is fixed at 128 cm. wave parameters in this data set are listed in Table I (case (D)). Notice that with the same experimental setup as case (A), the drift waves have the same azimuthal scale length, but are more broadband in this case (Fig. 11). This is possibly due to varied plasma conditions at different experimental run times, since a newly conditioned cathode was installed in the LAPD before this run. Beam FWHMs both in the active discharge and in the afterglow are obtained. In addition, beam profiles with no obstacle in the plasma are also measured, for

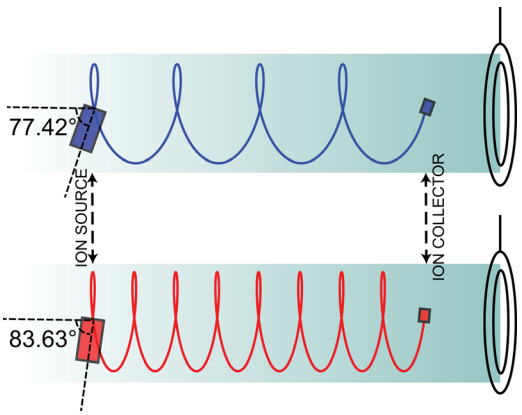


FIG. 10. (Color online) Schematic of the ion source and collector setup for two cases with different fast-ion time in the waves. (a) $T_f = 4\tau_{ci}$, (b) $T_f = 8\tau_{ci}$.

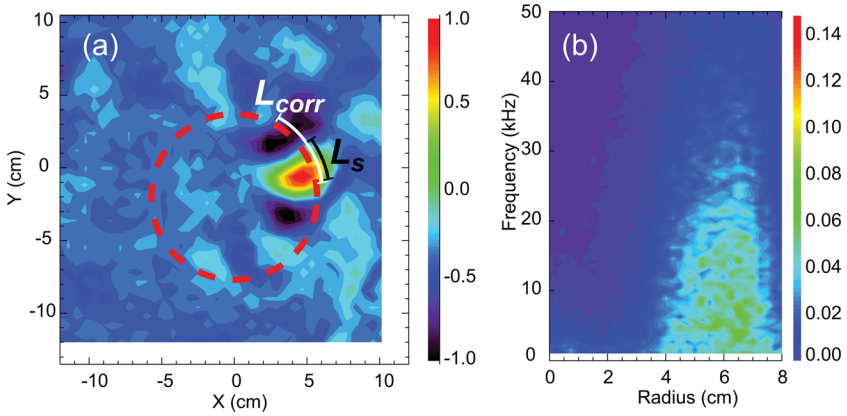


FIG. 11. (Color online) (a) Two-dimensional cross-field correlation function for $I_{sat}$ in case (D). (b) Contour of the spatially resolved wave spectrum for this case.

which the classical transport dominates. Both the beam FWHMs in the afterglow plasma and with no obstacle agree well with the simulated classical prediction of the MC code. However, in active-phase plasmas with large fluctuations, the beam FWHMs exceed classical levels (Fig. 12). To quantify the fast-ion diffusivity, the beam FWHM$^2$ is plotted against $T_f$, with the classical transport effect subtracted (triangles in Fig. 13). Since the fast ion gyro-period $\tau_{ci}$ is a constant, the fast-ion time-of-flight in the waves is also proportional to the number of gyrations it travels ($T_f = n_{gyro} \cdot \tau_{ci}$). The beam widths satisfy

$$W^2_{FWHM} - W^2_{classical} = 2\int_0^{T_f} D_W\, dt, \tag{3}$$

where $W_{FWHM}$ is the beam FWHM in waves, $W_{classical}$ is the beam FWHM due to classical transport, and $D_W$ is the fast-ion perpendicular diffusivity in waves. When plotted versus time, the slope of $(W^2_{FWHM} - W^2_{classical})$ indicates the amplitude of $D_W$ due to wave-particle interaction. A clear flattening in the data occurs for a gyration number of 6-8 and $T_f \sim 25$ ms. This indicates that $D_W(t)$ has a significant drop (in Fig. 13, $D_W(t) \sim 0$ at $\sim 25$ $\mu$s) with time and the transition from super-diffusive to sub-diffusive transport occurs. The time scale for transport to be sub-diffusive is estimated

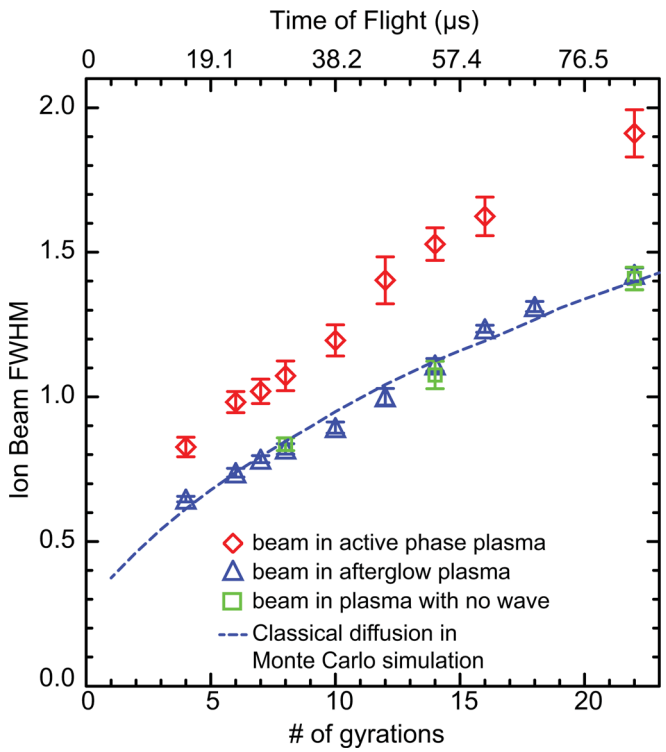


FIG. 12. (Color online) Fast-ion beam FWHM versus number of gyro-orbits in active discharge (diamonds), afterglow (triangles) and with the obstacle removed (squares). Beam FWHMs both in afterglow plasma and with obstacle removed indicate classical transport effect, and agree well with the Monte-Carlo simulation result. Beam FWHMs in active discharge reflect both classical and wave-induced transport.

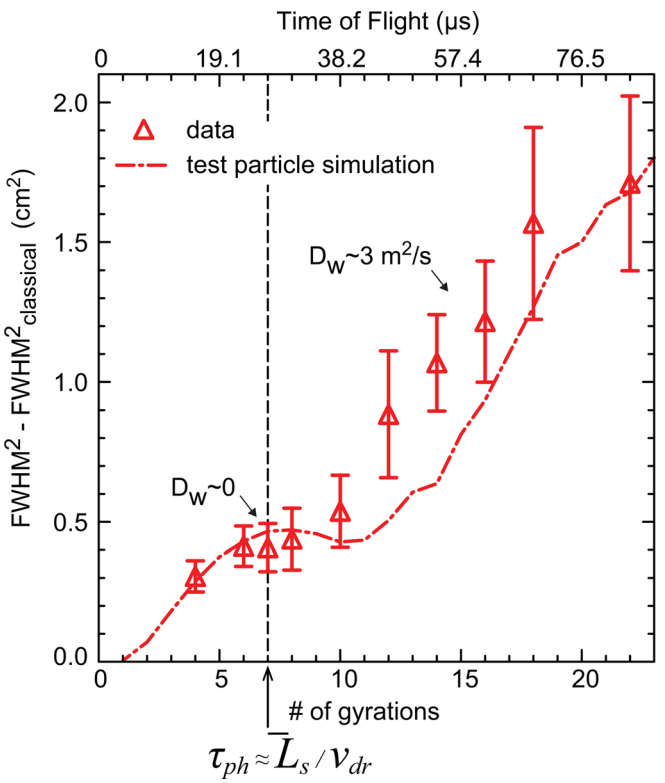


FIG. 13. (Color online) Spatial-temporal evolution of the fast-ion beam $FWHM^2 - FWHM^2_{classical}$ versus number of gyro-orbits for case (D). Data are collected with the collector at port 31 (triangles). A test-particle simulation result (red dash-dotted line) agrees well with the data.

as $\tau_{ph} \sim \bar{L}_s / v_{dr} \sim 26\,\mu s$, which agrees well with the observed sub-diffusive time scale.

### B. Test particle simulation results

Monte Carlo test-particle simulation results clearly predict that the sub-diffusive transport due to wave phase variations should be observable. First, a single particle GC position is followed in measured wave fields for 12 gyro periods (Fig. 14). The time-dependent wave structures used in this simulation is inferred by the measured cross-field correlation function of the $I_{sat}$ signal, and normalized to the maximum potential fluctuation amplitude. GC motion is initially ballistic (for $n_{gyro} \leq 4$), drifting in the same direction with nearly constant step length during each gyro-orbit. This indicates that when the fast ion orbit samples approximately the same wave phase, the corresponding beam transport is super-diffusive. At $n_{gyro} > 4$, phase changes of the background potential due to the diamagnetic and $E \times B$ drifts start to affect the particle trajectory, induces a backward GC drift, and the corresponding beam transport becomes sub-diffusive. A full simulation of the same effect is performed by following 50 000 test particles with random initial wave phases. The simulated beam FWHMs (dash-dotted line in Fig. 13) are normalized (to the maximum FWHM observed in experiment) and compared with experimental data. Flattening of $(W^2_{FWHM} - W^2_{classical})$ is also seen in the simulation, at the same time scale as the experimental result. This result agrees well with the theoretical explanation for sub-diffusive transport.

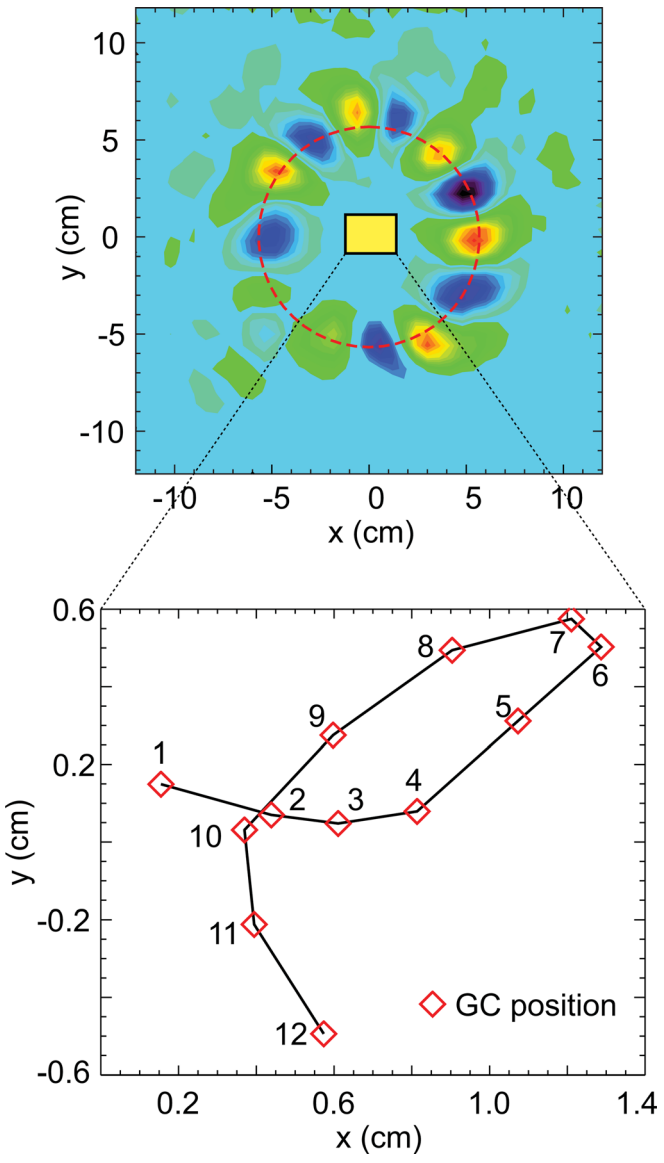


FIG. 14. (Color online) Simulation of the gyro-center drifts of a single particle during 12 gyro-periods in experimentally obtained wave structures.

## V. CONCLUSIONS

In this experimental work, turbulent waves associated with large density gradients and drift flow shear is observed. Direct measurement of fast ion non-classical spreading in the background waves quantifies the fast-ion cross-field transport due to interaction with low-frequency electrostatic wave potential fields. The background wave characteristics are modified by switching the working gas from helium to neon, and by altering the biasing voltage on the annular obstacle. Fast ion beam spreading in several typical cases shows that waves with larger spatial scale size (smaller mode number) cause more fast-ion transport; and with similar potential scale size, the coherent waves cause less fast-ion transport than turbulent waves. The difference in fast-ion transport is well explained by gyro-averaging effect: The averaged wave potential fluctuation amplitude is reduced due to the large fast-ion orbits, and the averaging effect depends on the coherency and structure scale sizes of the waves. When the fast ion interacts with the wave for most of a wave period, a transition from super-diffusive to sub-diffusive transport is observed, as predicted by diffusion theory. Simulation results of a Monte-Carlo particle following code show good agreement with the experimental data.

Several extensions of this experimental study are possible. Experimental study of fast-ion transport in waves with larger magnetic fluctuations (e.g., drift-Alfvén waves) is of great interest and predicted[30] to have different scaling to that in electrostatic waves. If the fast-ion collector is replaced with a diagnostic with excellent energy resolution, fast ion stochastic heating in turbulence also could be observed.

## ACKNOWLEDGMENTS

The authors gratefully acknowledge the assistance of Marvin Drandell, Zoltan Lucky, Bart Van Compernolle, Patrick Prybil, Brett Friedman, and Walter Gekelman for the experiment and helpful discussions. This work was supported by DOE and performed at the UCLA BaPSF basic plasma user facility supported by the NSF/DOE.

[1]T. Hauff, M. J. Pueschel, T. Dannert, and F. Jenko, Phys. Rev. Lett. **102**, 075004 (2009).
[2]G. Manfredi and R. O. Dendy, Phys. Rev. Lett. **76**, 4360 (1996).
[3]W. Zhang, Z. Lin, and L. Chen, Phys. Rev. Lett. **101**, 095001 (2008).
[4]M. Vlad, F. Spineanu, S.-I. Itoh, M. Yagi, and K. Itoh, Plasma Phys. Controlled Fusion **47**, 1015 (2005).
[5]W. W. Heidbrink and G. Sadler, Nucl. Fusion **34**, 535 (1994).

[6]W. W. Heidbrink, J. M. Park, M. Murakami, C. C. Petty, C. Holcomb, and M. A. V. Zeeland, Phys. Rev. Lett. **103**, 175001 (2009).
[7]S. Günter, G. Conway, S. daGraça, H.-U. Fahrbach, C. F. M. G. Muñoz, and T. Hauff, Nucl. Fusion **47**, 920 (2007).
[8]T. Suzuki, S. Ide, T. Oikawa, T. Fujita, and M. Ishikawa, and the JT-60 team, Nucl. Fusion **48**, 045002 (2008).
[9]J. M. McChesney, R. A. Stern, and P. M. Bellan, Phys. Rev. Lett. **59**, 1436 (1987).
[10]J. M. McChesney, P. M. Bellan, and R. A. Stern, Phys. Fluids B **3**, 3363 (1991).
[11]J. Bowles, R. McWilliams, and N. Rynn, Phys. Rev. Lett. **68**, 1144 (1992).
[12]R. McWilliams, M. K. Okubo, and N. S. Wolf, Phys. Fluids B **2**, 523 (1990).
[13]D. P. Sheehan, J. Bowles, and R. McWilliams, Phys. Plasmas **4**, 3177 (1997).
[14]A. Fasoli, A. Burckel, L. Federspiel, I. Furno, K. Gustafson, D. Iraji, B. Labit, J. Loizu, G. Plyushchev, P. Ricci, C. Theiler, A. Diallo, S. H. Mueller, M. Podestà, and F. Poli, Plasma Phys. Controlled Fusion **52**, 124020 (2010).
[15]G. Plyushchev, "Interaction of supra-thermal ions with turbulence in magnetized toroidal plasma," Ph.D. thesis (Ecole Polytechnique Fédérale de Lausanne, 2009).
[16]W. Gekelman, H. Pfister, Z. Lucky, J. Bamber, D. Leneman, and J. Maggs, Rev. Sci. Instrum. **62**, 2875 (1991).
[17]L. Zhao, W. W. Heidbrink, H. Boehmer, and R. McWilliams, Phys. Plasmas **12**, 052108 (2005).
[18]Y. Zhang, W. W. Heidbrink, H. Boehmer, R. McWilliams, S. Vincena, T. A. Carter, W. Gekelman, D. Leneman, and P. Pribyl, Phys. Plasmas **15**, 102112 (2008).
[19]Y. Zhang, W. W. Heidbrink, S. Zhou, H. Boehmer, and R. McWilliams, Phys. Plasmas **16**, 055706 (2009).
[20]S. Zhou, W. W. Heidbrink, H. Boehmer, R. McWilliams, T. A. Carter, S. Vincena, S. K. P. Tripathi, P. Popovich, B. Friedman, and F. Jenko, Phys. Plasmas **17**, 092103 (2010).
[21]S. L. Chen and T. Sekiguchi, J. Appl. Phys. **36**, 2363 (1965).
[22]Y. Zhang, H. Boehmer, W. W. Heidbrink, and R. McWilliams, Rev. Sci. Instrum. **78**, 013302 (2007).
[23]H. Boehmer, D. Edrich, W. W. Heidbrink, R. McWilliams, and L. Zhao, Rev. Sci. Instrum. **75**, 1013 (2004).
[24]J. R. Penano, G. J. Morales, and J. E. Maggs, Phys. Plasmas **7**, 144 (2000).
[25]J. E. Maggs and G. J. Morales, Phys. Plasmas **4**, 290 (1996).
[26]S. Vincena and W. Gekelman, Phys. Plasmas **13**, (2006).
[27]T. A. Carter and J. E. Maggs, Phys. Plasmas **16**, 012304 (2009).
[28]S. Zhou, W. W. Heidbrink, H. Boehmer, R. McWilliams, T. A. Carter, S. Vincena, and B. Friedman, "Sheared-flow induced confinement transition in a linear magnetized plasma," Phys. Plasmas (submitted).
[29]H. Naitou, T. Kamimura, and J. M. Dawson, J. Phys. Soc. Jpn. **46**, 258 (1979).
[30]T. Hauff and F. Jenko, Phys. Plasmas **15**, 112307 (2008).